ICA 2022
24th INTERNATIONAL CONGRESS ON ACOUSTICS
October 24(Mon) - 28(Fri), 2022 Gyeongju, Korea

PROCEEDINGS of the
24th International Congress on Acoustics

October 24 to 28, 2022 in Gyeongju, Korea

Scattering at the angles of polyhedral rooms: Application to stress-energy tensor conservation in Riemannian spaces

Jean-Dominique POLACK[(1)], Aidan MEACHAM[(2)], Roland BADEAU[(3)], Jean-Christophe VALIERE[(4)]

[(1)]Institut D'Alembert, Sorbonne Université, France, jean-dominique.polack@sorbonne-universite.fr

[(2)]Institut D'Alembert, Sorbonne Université, France, aidan@lam.jussieu.fr

[(3)]LTCI, TelecomParis, France, roland.badeau@telecom-paris.fr

[(4)]Institut PPrime, Université de Poitiers, France, jean.christophe.valiere@univ-poitiers.fr

ABSTRACT

Riemannian spaces with negative curvature constitute the proper setting for the distribution of images created by irregular polyhedral rooms with obtuse angles. The crucial parameter is the excess angle that arises around specific edges, called hinges, when first and second order images are considered, as it pilots the metric tensor of the space and all its geometrical properties. With the use of these geometrical properties, and complementing it with the uncertainty principle, we describe the scattering of wave packets around dihedral angles: it is proportional to the excess angle, and is best described in terms of the conservation of the stress-energy tensor. The basic elements for computing the scattering are given.

Keywords: Riemannian geometry, Polyhedral rooms, Scattering, Stress-energy tensor

1 INTRODUCTION

In a previous paper [1], we showed that the same mirroring technique as known for rectangular rooms can be applied to polygonal and polyhedral rooms of arbitrary shapes, leading to the tessellation of a Riemannian space with negative curvature. We were then able to show that the number of image sources increases exponentially with layer order, building a bridge between rooms with flat walls and generic mixing rooms with partially curved walls.

In the present paper, we take a further look at the implications of this tessellation, introducing the wave nature of the sound field in a room and the conservation of its energy and intensity, in order to explain scattering at corner and edges, while keeping mathematical complexity at minimum.

2 SCATTERING ON NON RECTANGULAR DIHEDRAL ANGLES

The proper setting for computing scattering on non rectangular dihedral angles is Riemannian geometry. We therefore first expose the basic principles of this geometry.

2.1 Riemannian geometry

We consider an n-dimensional space with its positive-definite metric tensor g_{ij} and the volume element $dV = \sqrt{g}dx^1 \dots dx^n$, where $g = \det g_{ij}$ is positive [2]. The infinitesimal distance element is given by:

$$ds^2 = g_{ij}dx^i dx^j \tag{1}$$

and we note g^{ij} the inverse matrix of g_{ij}. ∇_i is the covariant derivation with respect to x^i, which differs from the usual partial derivation ∂_i in a way that depends on the tensor rank. For example, for a function Φ:

$$\nabla_j \Phi = \partial_j \Phi = \Phi_j \tag{2}$$

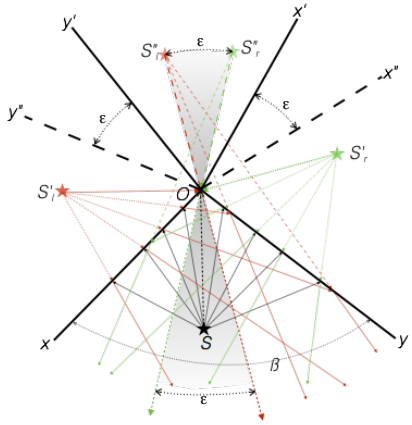

Figure 1. Reflection and scattering of sound rays on obtuse angle β. ε is the excess angle, since second order image angles overlap by ε.

but $\nabla_j \Phi_i = \partial_j \Phi_i - \Gamma^k_{ji} \Phi_k$ and $\nabla_j X^i = \partial_j X^i + \Gamma^i_{jk} X^k$, where X^i are the (contravariant) components of vector X and Γ^k_{ji} the Christoffel symbols linked to the derivatives of the elements of the metric tensor g_{ij}:

$$\Gamma^k_{ji} = \frac{1}{2} g^{kl} \left(\partial_j g_{il} + \partial_i g_{lj} - \partial_l g_{ji} \right) \tag{3}$$

Note that, unlike ordinary differentiations, covariant derivations do not commute.

2.2 Images rooms and obtuse angles

We consider the obtuse angle β of Figure 1 in a 2-dimensional Euclidean space. A sound source S (black star) emitting inside the angle emits rays in all directions. Some rays impinge on the left arm Ox of the angle and are reflected (red arrows). As the position of impact moves clockwise toward the apex, the reflected ray gradually moves upwards and eventually hits the right arm on which it is reflected once more. Finally, the ray impacts the apex of the angle (black upwards broken-line arrow).

In a similar fashion, some rays will impinge on the right arm Oy and be reflected (green arrows). As the position of impact moves anticlockwise toward the apex, the reflected ray gradually moves upwards and eventually hits the left arm on which it is reflected once more. Despite the continuity of the impinging rays around the apex, there is no continuity of the reflected rays, and this creates scattering.

In order to visualise the scattering, one needs to consider the images of the sources by reflection on the two arms of the angle. Let's call S'_l the image of the source on the left arm (red star), and S'_r the image on the right arm (green star); S''_l the left-most second order image (dim red star), and S''_r the right-most second order image (dim green star). Reflected rays on the arms of the angle are first emitted from the first order image sources S'_l and S'_r, then from the second order sources S''_l and S''_r when the reflected rays hit the opposite arm, until the rays emitted from the first-order image sources reach the apex (red and green dotted-line arrows). In that position, the rays emitted from the second order image sources do not coincide in direction, since they are emitted from two different image sources at angle ε with respect to the apex. Scattering therefore comes in to *fill the gap* between these two directions, and in fact beyond them. In other words, one must consider a continuum of image sources along the sector between S''_l and S''_r (grey sector), that is, one must rotate the second order image angle by ε from position $y''0x'$ to position $y'0x''$.

In fact, when rays rotate *clockwise* around the original source S, the reflected rays rotate *anticlockwise* around the first order source S''_l, and *clockwise* around the second order source S''_r. So, when the secondary source moves *clockwise* from S''_l to S''_r on Figure 1, the diffracted rays rotate *clockwise* around the apex, thus filling the grey sector with continuity of rotations at its boundaries.

In order to make the second order images coincide, one needs to embed Figure 1 in a 3-dimensional space

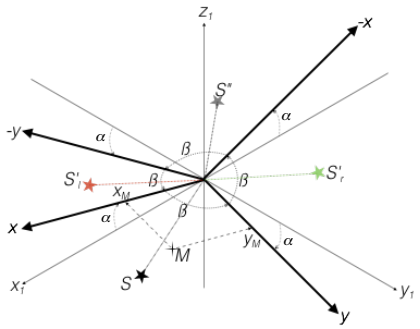

Figure 2. Embedding scattering on obtuse angle in 3-dimensional space. Angles α are vertical and measure deviations of angle arms from horizontal plane. Note that the two second order image sources coalesce in one single image source.

as in Figure 2. We call x_1, y_1, and z_1 the three Cartesian coordinates, and keep notations Ox and Oy for the arms of the original flat angular sector, which is now slanted so that angle β exactly projects on a right angle. As a consequence, Ox is elevated by angle α above Ox_1 and Oy is lowered by angle α below Oy_1; similarly, $O(-x)$ is elevated by angle α above $O(-x_1)$ and $O(-y)$ is lowered by angle α below $O(-y_1)$, so that the apex angle remains equal to β. In such a way, we obtain a *locally flat* space where rays are free to cross the borders between subsequent angular sectors without changing their direction.

2.3 Metric for obtuse angles

When the angle α is not null in Figure 2, that is, when $\beta > \pi/2$, the position of any point M in the system is given by its coordinates x and y, that are no longer orthogonal. In order to compute the corresponding infinitesimal distance element, one must project coordinates x and y on the Ox_1y_1 plane, then compute the vertical coordinate with equation:

$$z_1 = \tan\alpha(|\,x_1\,| - |\,y_1\,|) \tag{4}$$

valid for the four sectors of the system. With the convention $\mathrm{sgn}(0) = 0$, one obtains everywhere, even on the arms of the angles:

$$\begin{aligned} ds^2 &= dx_1^2 + dy_1^2 + dz_1^2 \\ &= (1+\tan^2\alpha)dx_1^2 + (1+\tan^2\alpha)dy_1^2 - 2\mathrm{sgn}(x)\mathrm{sgn}(y)\tan^2\alpha dx_1 dy_1 \end{aligned} \tag{5}$$

with $dx = \sqrt{1+\tan^2\alpha}dx_1$ and $dy = \sqrt{1+\tan^2\alpha}dy_1$, that is:

$$\begin{aligned} ds^2 &= dx^2 + dy^2 - 2\mathrm{sgn}(x)\mathrm{sgn}(y)\tfrac{\tan^2\alpha}{1+\tan^2\alpha}dxdy \\ &= dx^2 + dy^2 - 2\mathrm{sgn}(x)\mathrm{sgn}(y)\sin^2\alpha\, dxdy \end{aligned} \tag{6}$$

Simple projection on the plane Ox_1y_1 shows that $-\sin^2\alpha = \cos\beta$. Note that $\cos\beta < 0$ since $\pi/2 < \beta < \pi$ for obtuse angles. The last equation can therefore be written as:

$$ds^2 = dx^2 + dy^2 + 2\mathrm{sgn}(x)\mathrm{sgn}(y)\cos\beta\, dxdy \tag{7}$$

Using the embedding in the 3-dimensional space, distance elements ds are obviously continuous along a line that crosses one of the arms, implying that dx and dy are modified when the line crosses the arms. From the expression of ds^2, it is easy to deduce the metric tensor, its inverse, and its determinant:

$$g_{ij} = \begin{pmatrix} 1 & \mathrm{sgn}(x)\mathrm{sgn}(y)\cos\beta \\ \mathrm{sgn}(x)\mathrm{sgn}(y)\cos\beta & 1 \end{pmatrix} \tag{8}$$

$$g^{ij} = \frac{1}{\sin^2\beta}\begin{pmatrix} 1 & -\mathrm{sgn}(x)\mathrm{sgn}(y)\cos\beta \\ -\mathrm{sgn}(x)\mathrm{sgn}(y)\cos\beta & 1 \end{pmatrix} \tag{9}$$

$$g = \sin^2\beta \tag{10}$$

Note that g_{ij} and g^{ij} reduce to the identity matrix on the arms ($x = 0$ or $y = 0$) because of the convention $\mathrm{sgn}(0) = 0$, with $g = 1$.

Equation (3) then leads to the Christoffel symbols, that are all equal to 0, but for:

$$\begin{aligned} \Gamma^y_{xx} &= g^{yy}\partial_x g_{xy} = 2\delta(x)\mathrm{sgn}(y)\cos\beta \\ \Gamma^x_{yy} &= g^{xx}\partial_y g_{xy} = 2\mathrm{sgn}(x)\delta(y)\cos\beta \end{aligned} \tag{11}$$

where δ is the Dirac distribution, and where we have used the form for g^{xy} valid on the arms because $\delta(x)$, resp. $\delta(y)$, is null everywhere except on the arms $x = 0$, resp. $y = 0$;

It can further be shown [3] that the space has negative curvature at the apex O where it tends toward $4(\pi/2-\beta)$ for small values of $\pi/2-\beta$. Indeed, Regge [4] has shown that the curvature is equal to the total deficit angle at the apex $-\varepsilon = 2\pi - 4\beta$.

For a 3-dimensional obtuse dihedral angle, Fig 1 represents a projection of the rays on a plane perpendicular to the apical edge. But no equivalent of Fig 2 can be drawn, as the embedding takes place in a 4-dimensional space. Full computation shows that the local curvature remains null everywhere - flat space - except on the apical edge, called *hinge* by [4]. Note that hinges are subspaces of co-dimension 2 where excess angle is non null.

3 SCATTERING

3.1 Time-space metric

We now consider a 4-dimensional time-space with its metric tensor g_{ij} and the volume element $dV = \sqrt{|g|}dx^0 \ldots dx^3$, where $g = \det g_{ij}$ [2]. Here, g is *negative* as the first eigenvalue of the metric tensor is negative and equal to $-c^2$, where c is the speed of sound: its eigenvector corresponds to the time direction dx^0. The infinitesimal distance element is still given by equation (1):

$$ds^2 = g_{ij}dx^i dx^j \tag{12}$$

Therefore, covariant derivations and Christoffel symbols are still defined as in Sec. 2.3. More precisely, we have:

$$g_{ij} = \begin{pmatrix} -c^2 & 0 & 0 & 0 \\ 0 & 1 & \mathrm{sgn}(x^1)\mathrm{sgn}(x^2)\cos\beta & 0 \\ 0 & \mathrm{sgn}(x^1)\mathrm{sgn}(x^2)\cos\beta & 1 & 0 \\ 0 & 0 & 0 & 1 \end{pmatrix} \tag{13}$$

$$g^{ij} = \begin{pmatrix} -c^{-2} & 0 & 0 & 0 \\ 0 & \frac{1}{\sin^2\beta} & -\frac{\mathrm{sgn}(x^1)\mathrm{sgn}(x^2)\cos\beta}{\sin^2\beta} & 0 \\ 0 & -\frac{\mathrm{sgn}(x^1)\mathrm{sgn}(x^2)\cos\beta}{\sin^2\beta} & \frac{1}{\sin^2\beta} & 0 \\ 0 & 0 & 0 & 1 \end{pmatrix} \tag{14}$$

where β is one fourth of the total dihedral angle around the hinge, and with determinant $g = -c^2\sin^2\beta < 0$. g_{ij} and g^{ij} reduce to diagonal matrices on the arms, now denoted ($x^1 = 0$ and $x^2 = 0$), with all diagonal elements equal to 1 except $g_{00} = -c^2$ and $g^{00} = -c^{-2}$, and with $g = -c^2$. As for the Christoffel symbols, they are all

equal to 0, but for $\Gamma^2_{11} = 2\delta(x^1)\mathrm{sgn}(x^2)\cos\beta$ and $\Gamma^1_{22} = 2\mathrm{sgn}(x^1)\delta(x^2)\cos\beta$ (eq 11). It can be shown [3] that the time-space remains flat everywhere, except on the hinges, now given by the apical edges extended by the time laps.

3.2 Conservation of stress-energy tensor

The stress-energy tensor formalism was introduced into Acoustics by Morse and Ingard [5] in order to extend the wave equation by a set of conservation equations that are sum-upped in the conservation of the stress-energy tensor T^{ij}:

$$T^{ij} = \begin{pmatrix} T^{tt} & T^{tx} & T^{ty} & T^{tz} \\ T^{tx} & T^{xx} & T^{xy} & T^{xz} \\ T^{ty} & T^{xy} & T^{yy} & T^{yz} \\ T^{tz} & T^{xz} & T^{yz} & T^{zz} \end{pmatrix} \tag{15}$$

where T^{tt} is the total energy density; T^{tx}, T_{ty} and T_{tz} the sound intensity vector; and the remnant terms represent the spatial distribution of kinetic energy. Note that the stress-energy tensor is symmetrical.

The conservation of the stress-energy tensor can be written in terms of the covariant derivative of the stress-energy tensor as:

$$\nabla_i T^{ij} = \partial_i T^{ij} + \Gamma^i_{ik} T^{kj} + \Gamma^j_{ik} T^{ik} = 0 \tag{16}$$

that is ([2] p.54):

$$\frac{1}{\sqrt{|g|}} \partial_i (\sqrt{|g|} T^{ij}) + \Gamma^j_{ik} T^{ik} = 0 \tag{17}$$

or, after integration on a small 4-dimensional volume V with border ∂V:

$$\int_{\partial V} n_i T^{ij} dS + \int_V \Gamma^j_{ik} T^{ik} dV = 0 \tag{18}$$

In the last equation, n_i is the outgoing normal covector to the boundary, normalized by $n_i g^{ij} n_j = \pm 1$, with a negative sign for time boundaries.

With the form chosen for the metric tensor, the conservation of the stress-energy tensor reduces to:

$$\begin{aligned} \textstyle\int_{\partial V} n_i T^{i0} dS &= 0 \\ \textstyle\int_{\partial V} n_i T^{i1} dS &= -2\cos\beta \textstyle\int_V \mathrm{sgn}(x^1)\delta(x^2) T^{22} \sqrt{|g|} dx^0 dx^1 dx^2 dx^3 \\ \textstyle\int_{\partial V} n_i T^{i2} dS &= -2\cos\beta \textstyle\int_V \delta(x^1)\mathrm{sgn}(x^2) T^{11} \sqrt{|g|} dx^0 dx^1 dx^2 dx^3 \\ \textstyle\int_{\partial V} n_i T^{i3} dS &= 0 \end{aligned} \tag{19}$$

Note that the first line simply corresponds to the conservation of the total energy. For the two next lines, since $\cos\beta < 0$, when the stress-energy tensor crosses the arm Ox^2 of the angle, it receives a positive acceleration proportional to T^{22} in the x^1 direction; and when it crosses the arm Ox^1 of the angle, it receives a positive acceleration proportional to T^{11} in the x^2 direction; no acceleration occurs in the x^3 direction. The accelerations along the x^1 and x^2 directions, however, do not correspond to deviations of the direction of propagation since the space is flat everywhere but on the hinge. It only takes into account the change of coordinates across the arms of the angle.

3.3 Wave packets

Any ray issued from a sound source will have some thickness. This is simply due to the uncertainty principle (see for example [6]), which states that position and direction cannot be both determined with infinite precision. Note that this is not the case with the geometrical constructions of the previous Sections, where position and direction are simultaneously defined with infinite precision.

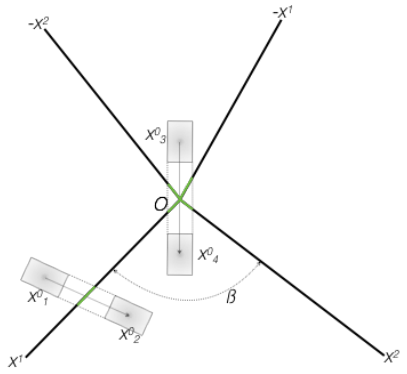

Figure 3. Wave packets crossing angle arms. Packet on the left crosses arm Ox^1 between x^0_1 and x^0_2; packet in the middle symmetrically crosses the two arms. Green lines mark the areas where deviations occur.

We now consider a wave packet, that is, a wave of finite extension, both along the direction of propagation and laterally, and we apply the stress-energy conservation equations (19) to it. We choose for integration a time interval over which the wave packet moves from one side of the angle arms to the other. Two cases are depicted in Figure 3.

The first wave packet is located in sector $(-x^2)Ox^1$ at time x^0_1. It is here defined by the projection of its distribution on the plane of Figure 3, where it is represented by a rectangle area with levels of grey proportional to the probability of presence of the wave packet. The size of the rectangle is chosen such that the components of the stress-energy tensor are negligible on its boundaries. As time increases, the wave packet moves at angle θ with respect to direction x^2 toward sector x^1Ox^2 in which it is located at time x^0_2. It crosses arm Ox^1 ($x^2=0$) in-between times x^0_1 and x^0_2, where it is deviated according to the second line of equation (19). In other words, the components of T^{ij} do not change, but for component T^{01}. Complete computation of the field [3] shows that the corresponding impulse exactly compensates for the coordinate change, so that the wave packet keeps on travelling in its initial direction.

This is not the case for the second wave packet, located in sector $(-x^1)O(-x^2)$ at time x^0_3 and moving to sector x^1Ox^2 at time x^0_4. It symmetrically crosses the arms $x^1=0$ and $x^2=0$ on its way. Since the function sgn changes sign around the origin O, the negative deviation compensates for the positive one on each axis, and no deviations occurs. However, if a larger part of the packet passes on one side of the origin, some deviation occurs in proportion of the offset. This case is not represented in Figure 3.

In both cases, direct calculation shows that T^{00} does not change when crossing arm Ox^1, as expected for energy conservation.

3.4 Ray scattering

Instead of thickening the rays by considering wave packets, an alternative is to thicken the hinges by low-pass filtering the Christoffel symbols on the arms (equation 3), and to look at the geodesics in the vicinity of the hinges. Indeed, differential geometry is a high-frequency theory, that does not account for wave-like phenomena. As a consequence, rays have infinitesimal thickness and are not deviated by hinges, unless they cross them.

We therefore propose to replace, in the Christoffel symbols of equations (11), $\delta(x)$ by the approximation $\sin kx/\pi x$, the weak limit of which is known to be the Dirac delta function when the wave number k tends towards infinity; and the function $\mathrm{sgn}(x)$ by the integral $-1+\int_{-\infty}^{x}(\sin kx/\pi x)dx$. We thus obtain:

$$\begin{aligned}\Gamma^y_{xx} &= \tfrac{\sin kx}{\pi x}\left[-1+2\int_{-\infty}^{x}\tfrac{\sin ky}{\pi y}dy\right]\cos\beta\\ \Gamma^x_{yy} &= \left[-1+2\int_{-\infty}^{x}\tfrac{\sin kx}{\pi x}dx\right]\tfrac{\sin ky}{\pi y}\cos\beta\end{aligned} \tag{20}$$

The crucial change introduced by these low-pass versions of the Christoffel symbols is the smooth and gradual transition from -1 to $+1$ that occurs across a hinge.

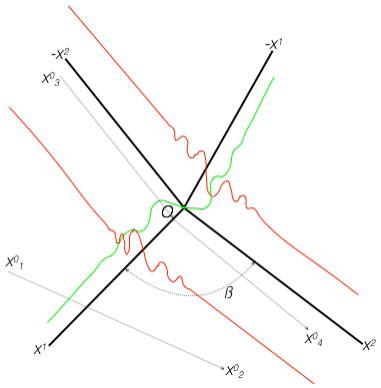

Figure 4. Ergodesics crossing angle arms. Geodesic x_1^0-x_2^0 crosses arm Ox^1 away from the apex and remains straight; geodesic x_3^0-x_4^0 crosses arm Ox^1 near the apex and is deflected. Green curve corresponds to low-pass sign function; red curves correspond to low-pass delta function.

In a Riemannian time-space, the equations of the geodesics are given by:

$$\frac{dv^k}{d\tau} = -\Gamma^k_{ij} v^i v^j \tag{21}$$

where τ is the proper time, $v^i = dx^i/d\tau$, and where $dv^k/d\tau$ is the acceleration in the direction x^k In the present case, the only non-zero accelerations are therefore along x^1 when crossing the arm $x^2 = 0$, and along x^2 when crossing the arm $x^1 = 0$. We therefore obtain:

$$\begin{aligned} \frac{dv^1}{d\tau} &= -\cos\beta \frac{\sin kx}{\pi x}\left[-1 + 2\int_{-\infty}^{x} \frac{\sin ky}{\pi y} dy\right]\left[v^2\right]^2 \\ \frac{dv^2}{d\tau} &= -\cos\beta \left[-1 + 2\int_{-\infty}^{x} \frac{\sin kx}{\pi x} dx\right] \frac{\sin ky}{\pi y}\left[v^1\right]^2 \end{aligned} \tag{22}$$

As a consequence, a ray that crosses one of the arms far from the hinge carries on in its original direction - ray x_1^0-x_2^0 in Figure 4 - since the integral of the sinc-function is equal to 1: the total impulse in the neighbourhood of the arm just compensates for the coordinate changes. But a ray that crosses one of the arms near the hinge, at a distance less than π/k - ray x_3^0-x_4^0 in Figure 4 -, undergoes an impulse that does not fully compensate for the coordinate change, with less compensation the nearer it comes to the hinge. In the limit case where the ray crosses on the hinge, the impulse vanishes and the ray is deviated by half the excess angle.

4 CONCLUSIONS

We have presented a geometrical theory that naturally accounts for scattering on the boundaries of a room. It introduces Riemannian spaces with negative curvature, which constitute the proper setting for the distribution of images created by non-rectangular rooms with obtuse angles, that is, created by irregular polyhedra. The crucial factor is the excess angle that arises around specific edges, called hinges, when first and second order images are considered, as it pilots the metric tensor of the space and all its geometrical properties, including its curvature.

Using the uncertainty principle, we were able to describe the scattering of wave packets around dihedral angles. The scattering is proportional to the excess angle, and can be described in terms of the stress-energy tensor, that is, in terms of energy conservation.

The present theory must now be developed to derive scattering coefficients from the distribution of hinges around a room. Most certainly, the excess angles are the main factors, complemented by the lengths of the hinges. But as schown in Sections 3.4, wave length also plays a rôle. Proper definition of scattering coefficients has long been missing for the application of the diffusion equation in Room Acoustics [7], despite some recent attempts [8].

There remains to introduce absorption in the present theory. Due to its geometrical nature, it cannot account for losses in its present form. The classical way to introduce absorption, which consider intensity flows inside the boundaries, cannot be used here without some adaptation. But accounting for losses should not proove difficult since absorption is easily described with the stress-energy tensor used in Sections 3.2 and 3.3, as shown in [9, 10].

REFERENCES

[1] Polack JD, Meacham A, Badeau R, Valière JC. Riemannian space tessellation with polyhedral room images. Proc 16th CFA; 11-15 April 2022; Marseille, France, 2022.

[2] Linet B. Notes de cours de relativité générale. Paris; 2004-5.

[3] Polack JD, Meacham A, Badeau R, Valière JC. Riemannian space tessellation with polyhedral room images. hal-03598258; 2022.

[4] Regge T. General Relativity without Coordinates. Nuovo Cimento. 1961;XIX:558-571.

[5] Morse PM, Ingard KU. Theoretical Acoustics. New York, USA; McGraw-Hill; 1968.

[6] Stephenson UM. An energetic Approach for the Simulation of Diffraction within Ray Tracing Based on the Uncertainty Relation. Acta Acust united Ac. 2010;96:516-535.

[7] Picaut J, Simon L, Polack JD. A mathematical model of diffuse sound field based on a diffusion equation. Acta Acust united Ac. 1997;83(4):614-621.

[8] Gül ZS. Exploration of room acoustics coupling in Hagia Sophia of Istanbul for its different states. J Acoust Soc Am., 2021;149(1):320-339.

[9] Dujourdy H, Pialot B, Toulemonde T, Polack JD. Energetic wave equation for modelling diffuse sound field - Applications to corridors. Acta Acust united Ac. 2017;103(3):480-491.

[10] Dujourdy H, Pialot B, Toulemonde T, Polack JD. Energetic wave equation for modelling diffuse sound field - Applications to open offices. Wave Motion. 2019;87:193-212.